


Designer quantum reflection from a microporeRomuald Kilianski * and Robert Bennett *University of Glasgow, University Avenue, G12 8QQ Glasgow, United Kingdom* (Received 21 October 2023; revised 18 January 2024; accepted 28 February 2024; published 18 March 2024)

We expand the theoretical toolbox for controllable quantum reflection by departing from a simple planar reflector. We introduce a circular hole (a micropore) of variable size, for which the electrostatic image potential can be exactly calculated. We combine this with two-dimensional simulations of wave-packet propagation at arbitrary angles of incidence to show that the quantum reflection probability can be tuned over a wide range of values.

DOI: [10.1103/PhysRevA.109.032812](https://doi.org/10.1103/PhysRevA.109.032812)**I. INTRODUCTION**

Quantum reflection is a counterintuitive effect in which an attractive surface-atom potential exhibits a repulsive behavior towards an incoming matter wave, i.e., the reflection occurs despite the absence of a classical turning point [1]. In other words, an atom that is accelerated towards a surface has a nonzero chance of reflection before coming into contact with it. This quintessentially wave behavior is familiar from classical theories, i.e., describing wave propagation in inhomogeneous media [2], but it is its quantum realization that has been the focus of research in recent decades.

Quantum reflection has been a widely studied phenomenon since the inception of quantum mechanics and was first placed into the realm of atom-surface interactions by Lennard-Jones and Devonshire [3]. In this context, the effect translates to an interference of probability waves; the unexpected outcome is that the reflection occurs at a threshold distance away from the surface. This effect was neatly demonstrated in a recent work [4], where a helium dimer was nondestructively reflected before it could reach the surface at which the potential would have been strong enough to dissociate its weak bond.

A wealth of literature exists on the theoretical treatment of quantum reflection [5–9], some recent publications have been concerned with reflection of atoms from rough surfaces [10,11] and some with antimatter (antihydrogen) reflecting off nanoporous materials [12] and liquid helium [13], while others have probed ultracold molecular collisions [14] and the effect of reflection in a cold Rydberg atomic gas with the use of single photons [15] and solitons [16]. Since the seminal paper by Shimizu [17], experimental realizations of quantum reflection from a solid surface have become abundant [18,19].

Some of the recent works include using quantum reflection to trap atoms in optical potentials [20], the reflection of Bose-Einstein condensates [21,22], metrological applications via observation of diffraction orders [23], and tests of quantum vacuum [24]. The diverse range of phenomena that can be probed via quantum reflection makes it an exciting and versatile tool in atomic physics.

The electromagnetic forces playing the key role in many realizations of quantum reflection belong to the class of phenomena collectively known as dispersion forces [25]. They arise as a result of the field fluctuations between two objects that do not possess a permanent electric or magnetic dipole moment. Amongst them are interatomic van der Waals forces, initially proposed by Eisenschitz and London [26], and interactions between larger bodies, introduced by Casimir [27] and Lifshitz [28]. A third, mixed, case describes the force between an atom or a molecule and a macroscopic object. It was first developed in the electrostatic regime by Lennard-Jones [29] and then extended to the retarded distances by Casimir and Polder (CP) [30]. Different naming conventions for the specific dispersion forces exist in the literature, but all are on a fundamental level expressions of the fluctuations of the vacuum, as described by quantum electrodynamics. We follow the convention adopted in Ref. [25] and refer to atom-body interactions—which are of central importance in this work—as CP forces.¹ Moreover, different distance regimes impose limits on the applicability of different theoretical descriptions of dispersion forces. Due to the finite speed of light, the information exchanged on scales much larger than the transition wavelength of an atom will suffer a phase delay, thus experiencing retardation effects. In this paper, we consider the short, nonretarded regime—this is the domain of applicability of the electrostatic potential we will use.

Control of dispersion forces therefore allows control of quantum reflection. Research so far in this direction has

*r.kilianski.1@research.gla.ac.uk

Published by the American Physical Society under the terms of the Creative Commons Attribution 4.0 International license. Further distribution of this work must maintain attribution to the author(s) and the published article's title, journal citation, and DOI.

¹Some authors refer to any far-field dispersion interaction involving at least one atom as Casimir-Polder, while others use the convention employed here where Casimir-Polder refers to the interaction (at any distance) between an atom and the macroscopic body.

mainly been centered around investigating the versatility of graphene as a material, enabling the control of the atom-surface potential. The work in Refs. [31–33] explores the use of a magnetic field to alter the properties of a sheet of graphene, effectively changing the CP interaction potential. Some other investigations in the graphene-based systems include carrier doping [34], the application of mechanical strain [35], and plane stacking arrangements [36]. Moreover, various experimental applications have already been realized [37–39], paving the way for future uses in nanotechnology. Other materials in the graphene family have also been probed in the context of quantum reflection and its connection with topological phase transitions, stimulated by electric fields [40]. The application of electric fields has equally been successful in controlling quantum reflection in silicon gratings—outside of the realm of graphene—as experimentally shown in Ref. [41].

In this work we choose to investigate the paradigmatic case of a perfectly reflecting plate, but with a twist. We introduce a circular hole (a micropore) to our metallic plate. By changing the diameter of the hole, we are able to reduce the potential gradient in its immediate neighborhood and in turn, gain control of the strength of reflection of, for example, a matter wave passing through. Despite the presence of the micropore, which one might expect to allow full transmission of a highly collimated matter wave, the atom continues to reverse its motion at the threshold. For the majority of the cases considered, the rate of reflectivity is reduced compared to the case of no hole. This apparent “antitunneling” event, where in the region of absence of a material surface one would expect the atom to propagate through, renders a curious addition to an already counterintuitive quantum phenomenon. After incorporating the variable hole diameter, we extend the space of control parameters by including the angle of incidence and test their impact on the reflectivity. Due to the nonseparability of the potential, we numerically solve the time-dependent Schrödinger equation (TDSE), for ^3He and Na , both modeled as a Gaussian pulse propagating towards a plate with a hole.

This paper is organized as follows. We first discuss the conditions for the quantum reflection, considering a single degree of freedom. Second, in Sec. II we present the exact, two-dimensional, nonseparable potential for a perfectly reflecting plate with a hole from Ref. [42]. We then modify its domain to enable numerical simulations of quantum reflection by solving the TDSE using a spectral, split-step method. We then proceed to present the results in Sec. III, showcasing the dependence of the reflectivity upon the hole diameter and angle of incidence. In the Appendix we validate our algorithm for the case of normal incidence and examine the influence of the grid size on convergence.

II. PROCEDURE

A. Quantum reflection in one dimension and two dimensions

Quantum reflection has been studied overwhelmingly as a one-dimensional problem. The atom-surface forces between matter and a regular macroscopic object depend on the normal distance between them, resulting in the consideration of only a single degree of freedom. The conditions for the quantum

reflection in one dimension (1D) are determined by the properties of the traveling matter wave. If $V(x)$ is an arbitrary potential varying in the x direction, m is the particle’s mass, and k_0 is its k vector at $x \rightarrow \infty$ ($V \rightarrow 0$), the local wave vector of the particle k ,

$$k = \sqrt{k_0^2 - 2mV(x)/\hbar^2}, \quad (1)$$

is required to change abruptly on the scale of its de Broglie wavelength λ_{dB} for quantum reflection to occur [17]. This significant change can be mediated by an interaction potential, V , that grows rapidly as the atom approaches the surface. CP forces with their $1/r^3$ or $1/r^4$ dependence are therefore ideal for inducing quantum reflection. The majority of theoretical investigations into quantum reflection elude fully analytical treatment and rely on semiclassical approaches such as WKB approximation [43,44]; however, these are not applicable in higher dimensions for nonseparable potentials [45]. Only until recently [45], all efforts have been confined to the one-dimensional case, in which a time-independent Schrödinger equation is solved for a given potential, and the reflectivity is obtained as a ratio of amplitudes of counterpropagating waves. Quite understandably, a reliable method of solving a two-dimensional quantum reflection problem is a recent occurrence due to the computationally expensive nature of such a setup. Inspired by the aforementioned work by Galiffi *et al.* [45], we apply a time-dependent approach to solve a pulse propagation problem in the vicinity of a perfectly reflecting plate with a hole.

B. Potential function

The geometry we have chosen is a smooth metal plate with a hole in its center, as shown in Fig. 1. The exact electrostatic potential for this situation was calculated by Eberlein and Zietal [42] by the means of a Kelvin transform [46]. Defined in cylindrical coordinates, $V(\rho, \phi, z)$, and for a hole diameter, d , their result can be written as

$$V(\rho, z; d) = -\frac{1}{16\pi^2\epsilon_0} (\Xi_\rho \langle \mu_\rho^2 \rangle + \Xi_\phi \langle \mu_\phi^2 \rangle + \Xi_z \langle \mu_z^2 \rangle). \quad (2)$$

The $\langle \mu_i^2 \rangle$ terms are the expectation values of the i th cylindrical component of the dipole moment operator, and the coefficients Ξ_i are

$$\Xi_\rho = \frac{d\rho^2}{R_+^5 R_-^5} (P^2 - d^2 z^2) + \frac{d^3}{6R_+^3 R_-^3} + \frac{1}{4z^3} \left[\frac{\pi}{2} + \arctan\left(\frac{P}{dz}\right) + \frac{dz}{R_+^4 R_-^4} Q_-^2 P \right], \quad (3)$$

$$\Xi_\phi = \frac{d^3}{6R_+^3 R_-^3} + \frac{1}{4z^3} \left[\frac{\pi}{2} + \arctan\left(\frac{P}{dz}\right) + \frac{dz}{R_+^2 R_-^2} P \right], \quad (4)$$

$$\Xi_z = \frac{d}{R_+^5 R_-^5} \left(z^2 Q_+^2 - \frac{d^2}{4} Q_-^2 \right) + \frac{d^3}{6R_+^3 R_-^3} + \frac{1}{2z^3} \left[\frac{\pi}{2} + \arctan\left(\frac{P}{dz}\right) + \frac{dz}{R_+^2 R_-^2} Q_- + \frac{2d\rho^2 z^3}{R_+^4 R_-^4} P \right], \quad (5)$$

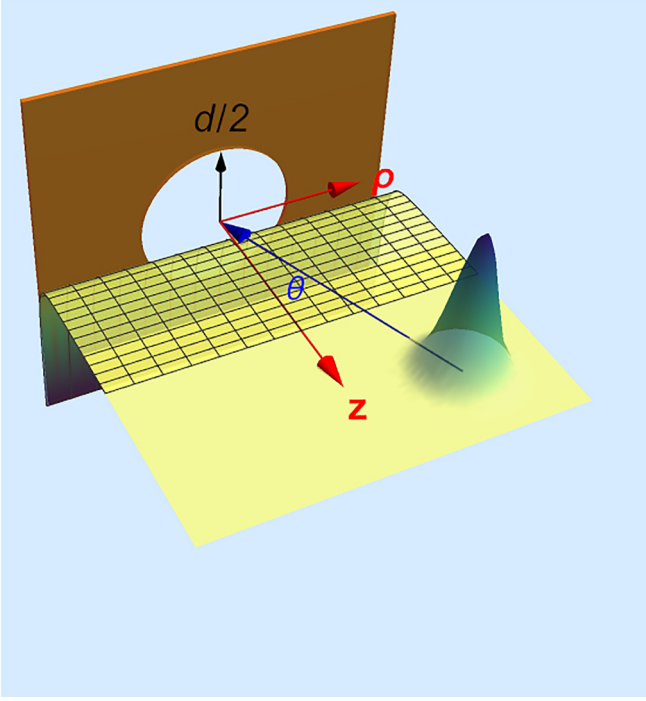


FIG. 1. A schematic illustration of the setup. A pulse travels towards the plate at the incidence angle θ , being influenced by the attractive potential $U(\rho, z; d)$. The potential was originally derived in the cylindrical coordinates but we discard the ϕ -dependent component due to the uniaxial invariance and treat ρ and z as Cartesian coordinates. The hole is characterized by a diameter of length d .

where we used the following shorthand notations:

$$P = \rho^2 + z^2 - \frac{d^2}{4}, \quad (6)$$

$$Q_{\pm} = \rho^2 \pm z^2 \pm \frac{d^2}{4}, \quad (7)$$

$$R_{\pm} = \left[\left(\rho \pm \frac{d}{2} \right)^2 + z^2 \right]^{1/2}. \quad (8)$$

For the hole diameter d approaching zero, $V(\rho, z; d)$ reduces to the form $\propto z^{-3}$ —a potential varying only in one direction, thus assuming the form familiar from 1D. Equation (2) describes the energy shift of an atom with an arbitrarily oriented dipole; in our case, we choose the dipole to always be pointing in the direction of the atom's motion. We therefore parametrize the dipole moment as

$$\boldsymbol{\mu}_{\rho} = (\mu_x \cos \phi + \mu_y \sin \phi) \hat{\rho}, \quad (9)$$

$$\boldsymbol{\mu}_{\phi} = (-\mu_x \sin \phi + \mu_y \cos \phi) \hat{\phi}, \quad (10)$$

$$\boldsymbol{\mu}_z = \mu_z \hat{z}, \quad (11)$$

where $\hat{\rho}$, $\hat{\phi}$, and \hat{z} are the usual cylindrical unit vectors and $\boldsymbol{\mu} = (\mu_x, \mu_y, \mu_z)$ is the dipole moment vector in Cartesian coordinates. By choosing a plane of motion where $\mu_y = 0$ and $\mu_x > 0$, we notice that $\phi = \arctan(y/x) = 0$. Now, by defining the angle $\theta = \arctan(x/z)$, we can write the remaining dipole components as $\mu_x = |\boldsymbol{\mu}| \sin \theta$ and $\mu_z = |\boldsymbol{\mu}| \cos \theta$. This

allows us to write the energy shift $V(\rho, z; \theta, d)$ as

$$\begin{aligned} V(\rho, z; \theta, d) &= -\frac{1}{16\pi^2 \epsilon_0} (\Xi_{\rho} \langle |\boldsymbol{\mu}|^2 \rangle \sin^2 \theta + \Xi_z \langle |\boldsymbol{\mu}|^2 \rangle \cos^2 \theta) \\ &= -\frac{C_3}{\pi} (\Xi_{\rho} \sin^2 \theta + \Xi_z \cos^2 \theta), \end{aligned} \quad (12)$$

where $C_3 = \langle |\boldsymbol{\mu}|^2 \rangle / 16\pi \epsilon_0$, with $\langle |\boldsymbol{\mu}|^2 \rangle$ being the square of the expectation value of the dipole moment, and following Refs. [45,47], we set $C_3 = 4.0 \times 10^{-50}$ J, which describes the interaction between ^3He and a Au plate. By fixing the plane of propagation, ρ and z effectively become Cartesian coordinates, but for the sake of clarity and continuity we retain the cylindrical labels. The fixed, relative relationship between Ξ_z and Ξ_{ρ} components, such that the atom's dipole always points in the direction of motion, is described by the angle of incidence θ and is schematically shown in Fig. 1.

C. Extended potential

Any experiment aiming to measure quantum reflection needs to come up with a way of isolating it from the classical reflections induced by the short-range repulsion very close to the surface (for example, using the bond dissociation technique in Ref. [4]). In our numerics we do this by simply not including the short-range repulsion (which would be implemented by letting $V \rightarrow \infty$ at the plate) and considering only the effects of the potential $V(\rho, z; \theta, d)$ as shown. This means that any reflections that occur are necessarily quantum in nature. To implement this, we split our computational domain into two halves, with the plate envisaged as being in the middle at $z = 0$. On the right-hand side, the potential is $V(\rho, z; \theta, d)$, while on the left, we artificially continue the potential to the edge of the domain in the way we explain shortly. Since the potential $V(\rho, z; \theta, d)$ experiences an unphysical singularity at $z = 0$, we choose a small enough distance ϵ as a cutoff point (as was implemented, for example, in Ref. [48]). This length needs to be sufficiently small so the resulting potential still reaches close enough to the surface to be relevant to electrostatic interactions—varying ϵ impacts the reflectivity and this is discussed in the Appendix where we test different lengths ϵ . We now proceed to define a new piecewise potential function V_C as

$$V_C = \begin{cases} V(\rho, z; \theta, d), & z > \epsilon, \\ -\frac{3V_0}{2\epsilon^2} z^2 + \frac{5V_0}{2}, & 0 \leq z \leq \epsilon \text{ and } |\rho| < \frac{d}{2}, \\ \frac{5V_0}{2}, & z < 0 \text{ and } |\rho| < \frac{d}{2}, \\ V_{<}, & \text{otherwise,} \end{cases} \quad (13)$$

where $V_0 \equiv V(0, \epsilon; \theta, 0)$ and $V_{<} \equiv V(0, \epsilon; \theta, d)$. The extended potential in the region $0 \leq z \leq \epsilon$ is essentially a function of z only. The change of the potential's landscape in the ρ direction induced by the introduction of the hole is symmetrical, and significant only at z near ϵ . We thus create a gap in the continued part of the potential in the positive and negative ρ directions, at $z = \epsilon$, to account for the vanishing potential gradient at the hole's center. For $z < \epsilon$ and beyond the gap, V_C is invariant in ρ ; for a wave packet traveling in

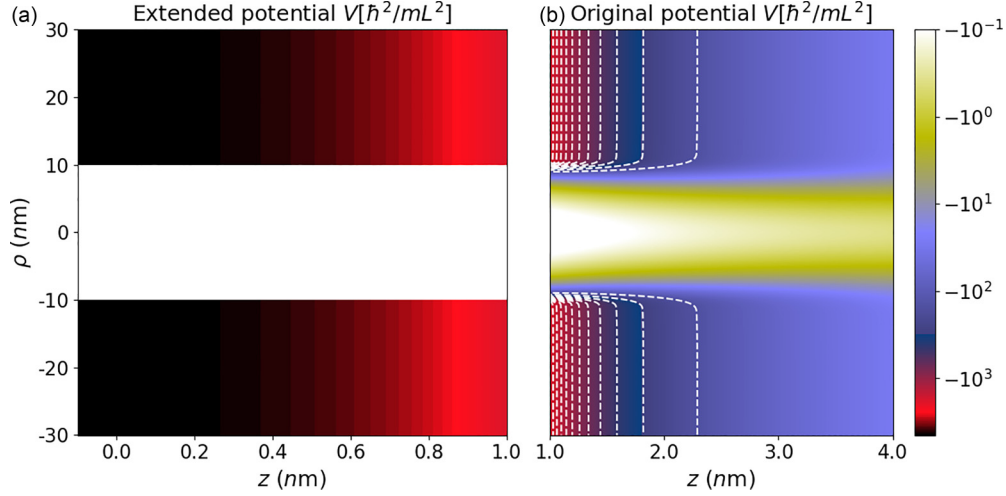


FIG. 2. (a) Potential V for an atom of ${}^3\text{He}$, continued beyond the $z = \epsilon$ distance through to the negative z values where it reaches a constant value. (b) The behavior of the original potential V from the cutoff point at $z = \epsilon$. The unit $\hbar^2/mL^2 = 138.5$ neV.

the ρ direction, such an abrupt change along the ρ axis will have an effect on its motion. However, this is inconsequential for our purposes as this occurs in the continued part of the potential and does not influence the reflection in the normal direction. The original potential along with its extension is shown in Fig. 2. We plot the regularized potential at a $\rho = 0$ slice for different diameters d in Fig. 3.

D. Evolution of the system

We aim to solve a dimensionless time-dependent Schrödinger equation (TDSE):

$$-\frac{1}{2}\nabla^2\Psi(\mathbf{r}, t) + V(\mathbf{r})\Psi(\mathbf{r}, t) = i\partial_t\Psi(\mathbf{r}, t). \quad (14)$$

We solve Eq. (14) by taking advantage of an open source library [49]—a solver utilizing the split-step Fourier technique, also known as the beam propagation method (BPM) [50]. Determined by the natural units and the choice of length scale $L = 1 \mu\text{m}$, the energy unit in which the system in Eq. (14) is solved is \hbar^2/mL^2 , where m is the actual mass of the atom in SI units. We adapt the source code of Ref. [49] to include our extended potential function V_C , and we solve the TDSE for a range of chosen angles of incidence θ and diameters

d . In Table I, we specify the simulation-specific parameters for ${}^3\text{He}$ and Na, to which we refer throughout the text. At $t = 0$, we define $\Psi(\mathbf{r}_0, 0)$ to be a Gaussian with the spread (standard deviation) in z and ρ , respectively, $\sigma_z = \sigma_\rho = 10$ nm ($1 \mu\text{m}$), for ${}^3\text{He}$ (Na). The initial location is situated at $\mathbf{r}_0 = \{r \cos \theta, r \sin \theta\}$, where θ is the angle of incidence and r is chosen to be 40 nm ($4 \mu\text{m}$). We impart on the pulse momentum $p_0 = \sqrt{2mE_0}$, where m is the mass of ${}^3\text{He} = 3.016$ amu (Na = 22.99 amu) and E_0 is the kinetic energy. The computational domain is surrounded by an absorbing boundary, where the solver makes V imaginary. Additionally, periodic boundary conditions are enforced and any pulse that “leaks” through the absorbing medium reappears at the starting point. We can stop that from happening if we choose a “sensible” stopping point, an appropriate duration of propagation turns out to be $t_f = 0.12$ (0.21). The resulting $\Psi(\mathbf{r}, t_f)$ contains the information about the spread of the pulse at time t_f . To extract the information about the reflected part of the pulse, we simply integrate the normalized squared amplitude of the wave function along the ρ axis and the positive z direction. This way, we find the proportion of the pulse traveling in the positive z direction at t_f , which we call reflectivity $R(t_f)$,

$$R(t_f) = \int_{-\infty}^{\infty} d\rho \int_0^{\infty} dz |\Psi(\mathbf{r}, t_f)|^2. \quad (15)$$

An alternative, very similar treatment is to Fourier transform $\Psi(\mathbf{r}, t_f)$ and integrate along the momentum in the ρ direction and the positive momentum in the z direction; the

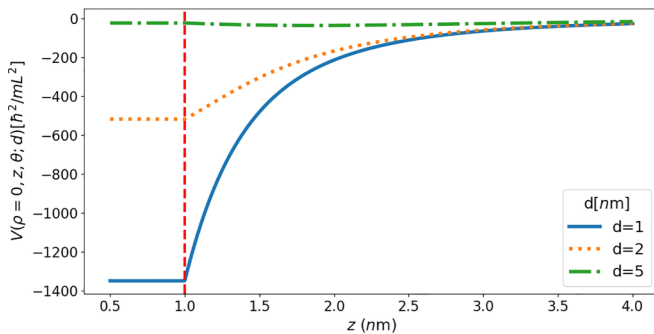


FIG. 3. The extended potential V_C at $\rho = 0$ for three different hole diameters d . The red dashed line shows the cutoff point ϵ . The larger the hole diameter is, the flatter the potential gradient becomes near the center.

TABLE I. Parameters in natural units (SI units) used in the simulations.

Atom	${}^3\text{He}$	Na
Array dims.	15×15 ($150 \times 150 \text{ nm}^2$)	25×25 ($25 \times 25 \mu\text{m}^2$)
Energy E_0	1.13×10^3 (156 μeV)	665.70 (1.21 neV)
Time t_f	0.12 (0.51 ps)	0.21 (0.115 μs)
Cutoff ϵ	0.1 (1 nm)	0.1 (100 nm)
C_3	1.8 (4.0×10^{-50} J)	4.21 (1.2×10^{-48} J)

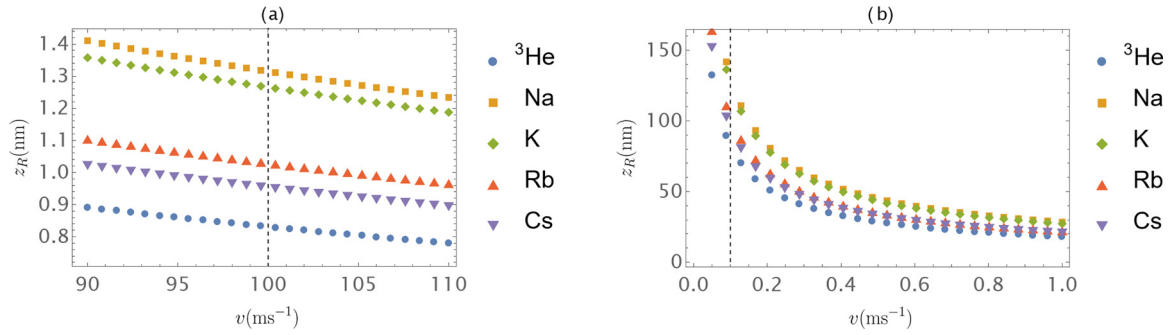


FIG. 4. The distance z_R at which a quantum reflection occurs as a function of incident velocity, for various atoms. z_R has been calculated as a location of the maximum of a Badlands function. The plot in panel (a) shows the regime of applicability of the ^3He atom, with the dashed line marking its velocity ($v = 100 \text{ m s}^{-1}$); the same in panel (b) but for the Na atom ($v = 0.1 \text{ m s}^{-1}$).

reader can see Refs. [45,48] for further details. We found this technique to produce almost identical results with the exception of cases where a pulse travels at grazing angles of incidence, causing the positive momentum to be poorly defined.

We notice that the addition of the hole significantly flattens the gradient of the potential in the region corresponding to its diameter across the whole domain, as seen in Fig. 2(a). This serves as basis for expecting suppressed reflectivity across those regions.

III. RESULTS AND ANALYSIS

Since we have based our investigations on using an electrostatic potential, we need to confirm that the reflection is happening at distances appropriate to the short-range, non-retarded CP interaction. The electrostatic regime is usually accessible through high kinetic energies, where in the case of helium, the particle's speed $v \approx 300 \text{ m s}^{-1}$, as shown experimentally in, for example Ref. [19]. In this work, we wish to look at the reflection of ^3He at nonretarded distances, traveling at a velocity of $v \approx 100 \text{ m s}^{-1}$, ensuring that the reflection location falls inside the reach of the electrostatic interaction. We note that if we were to consider an arbitrary atom, the short-distance regime of the reflection could be achieved by tuning into an appropriate energy range, along with choosing a surface whose effects are encoded by the C_3 coefficient.

We can confirm the suitability of our setup to an electrostatic regime by reducing our problem to a single dimension (normal incidence at $\rho = d = 0$) and examining the location of quantum reflection. A well-known estimation of the order of magnitude of this distance (in one dimension) can be inferred from the so-called Badlands function [44,51]—which we denote $Q(z)$ —as demonstrated, for example, in Refs. [52] and [12]. The significance of $Q(z)$ to the problem at hand lies in its relation to the modified Schrödinger equation (here E is the kinetic energy, m is the atomic mass, and $V(z)$ is an arbitrary potential function depending on the atom plate separation z)

$$\psi''_{\text{WKB}}(z) + \frac{2m}{\hbar}[E - V(z) + Q(z)]\psi_{\text{WKB}}(z), \quad (16)$$

for which the WKB approximation ψ_{WKB} is an exact solution. The dimensionless form of the Badlands function $Q(z)$ can be

written as

$$Q(z) = \frac{4[V(z) - E]V''(z) - 5[V'(z)]^2}{32[E - V(z)]^3}, \quad (17)$$

where $V(z) \equiv V(0, z; 0, 0)$ is the one-dimensional potential function, E is the kinetic energy, and primes denote differentiation with respect to z . The peaks of $Q(z)$ coincide with regions where the WKB approximation breaks down (distances at which the wave vector experiences drastic changes), revealing the approximate position at which the quantum reflection occurs. Thus, by finding the location of a maximum of the Badlands function for a given configuration (choice of an atom and its velocity), we can check the applicability of a given regime. We have found the peaks of the Badlands function for the case of a perfect reflector for ^3He along with Na, K, Rb, and Cs, using the C_3 coefficients for the alkali metals from Ref. [53]. The results are shown in Figs. 4(a) and 4(b). For all elements in Fig. 4(a), we notice a linear relationship between the velocity v and the approximate distance of reflection z_R ; across the range of velocities, the difference between atoms' reflection distances for a given v is less than a nanometer. The regime of validity of the electrostatic interaction is determined by the dominating transition frequency (wavelength λ) of an atom, such that $z_R \ll \lambda$ (in the case of ^3He , $\lambda = 9.3 \text{ nm}$ [48]). We are thus considering a reflection distance which is approximately ten times smaller than the wavelength λ , motivating us to discard any contribution that might be arising over the scale of retarded distances ($z \gg \lambda$). We believe this to be a justifiable assumption for ^3He , following the work in Ref. [45], whose use of the electrostatic potential influences our own method. Additionally, the lowest limit for the cutoff point ϵ producing convergent results for all angles θ was found to be $\epsilon = 1 \text{ nm}$. This situates it within the approximate region where the Badlands function predicts the reflection to occur, yet it still allows for the full interaction to play out—the pulse starts reversing its motion before the cutoff point. For the case of the alkali-metal atoms (K, Rb, Cs) along with Na as shown in Fig. 4(b), the distance at which the quantum reflection occurs also falls in the nonretarded regime. In the case of Na, the distance z_R is approximately five times smaller than its transition wavelength, $\lambda \approx 590 \text{ nm}$. Our model is built on the condition of a perfectly reflecting sheet where the electric field disappears on the surface. If however, one wanted to relax this assumption and consider

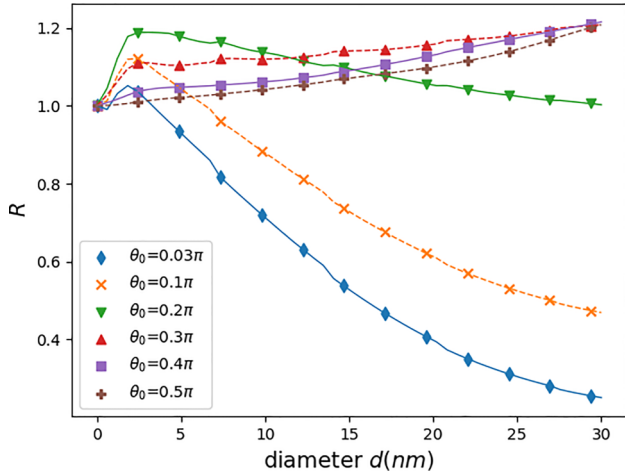


FIG. 5. Explicit dependence of normalized reflectivity R on the diameter of the hole, d , for a selection of angles θ for an atom of ${}^3\text{He}$ traveling at $v = 100 \text{ m s}^{-1}$.

penetration depth for real metals, proportional to the reciprocal of the square root of frequency [54], the skin-depth would be approximately on the order of magnitude of the predicted quantum reflection distance for ${}^3\text{He}$ and an order of magnitude smaller for Na. Thus, for ${}^3\text{He}$ the physical condition that the reflection distance is much greater than the penetration depth is not necessarily satisfied, so our results for ${}^3\text{He}$ should be taken as indicative only to aid comparison with previous theoretical works.

Having confirmed the validity of the one-dimensional electrostatic model for several atoms, we carry out two-dimensional simulations for an atom of ${}^3\text{He}$ and Na; in both cases we vary the incidence angle θ and the hole diameter d . The normalized—with respect to the case of $d = 0$ (no hole)—results for ${}^3\text{He}$ (Na) are plotted in Fig. 5 (Fig. 7), showcasing the relationship between the hole diameter d and the reflectivity R . In the case of ${}^3\text{He}$, we notice an initial

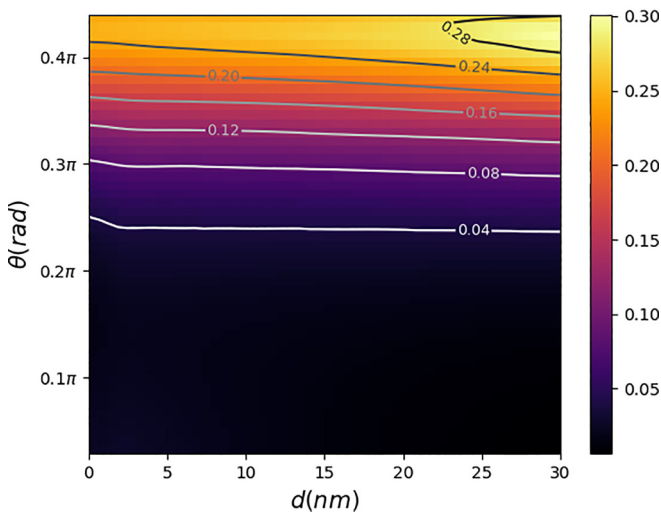


FIG. 6. Reflectivity R as a function of the diameter of the hole, d , and the angle of incidence θ for an atom of ${}^3\text{He}$ traveling at $v = 100 \text{ m s}^{-1}$.

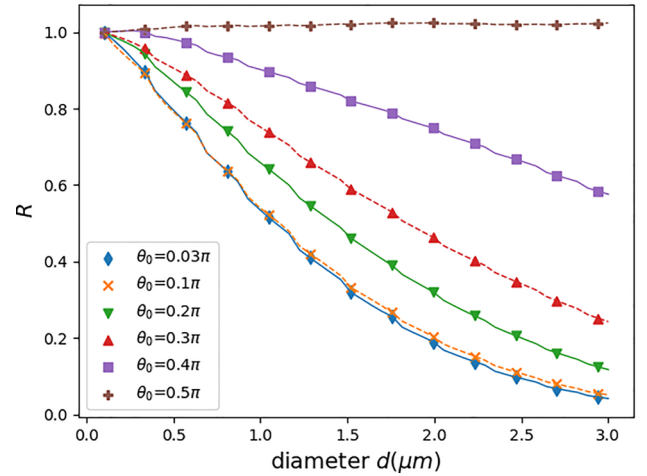


FIG. 7. Explicit dependence of reflectivity R on the diameter d for an atom of Na traveling at $v = 0.1 \text{ m s}^{-1}$.

increase in reflectivity compared to the case of no hole for all angles of incidence, suggesting a resonancelike interaction between the pulse and the opening. For an atom traveling at a small incidence angle ($\theta < 0.3\pi$), the effects of this behavior diminish with the increasing diameter of the hole. The bigger the overlap between the hole's cross section and the arc that angle θ subtends is, the larger portion of the pulse experiences reduced strength of the potential gradient. For larger angles of incidence ($\theta \geq 0.3\pi$), the increasing trend is sustained throughout all diameters d . The density plot of the reflectivity for the parameter space for ${}^3\text{He}$ is shown in Fig. 6. In the case of the Na atom (Fig. 7), the effect of the resonance is smaller—we observe a slight increase in reflectivity for the angle $\theta = 0.4\pi$. Moreover, at θ close to 0.5π , the approximately constant reflectivity experiences a slight enhancement across the range of the d values. In this case, the atom traverses parallel to the plate and its direction of motion is unaffected by the presence of the hole; however, its spread in the perpendicular direction is modulated by the opening. As shown in Fig. 8, we notice the diminishing influence of the hole on pulses that travel at the grazing angle of incidence.

Additionally, independent of the hole diameter d , in the case of each atom we observe a periodic behavior along the θ axis. The ratio of the reflected wave to the incoming one is modulated by the coupling between the potential's respective dependencies on ρ and z . Interestingly, when the diameter of the hole approaches zero—which nullifies nonperpendicular dependence—we still observe the periodic behavior. Since this occurs for both atoms, we have examined the animations of the respective simulations and have found them to be describing the correct values of the reflectivity—we expand on this point in the Appendix. We suggest that the reason behind this phenomenon lies in the self-interference of the wave packet. As it strikes the potential barrier, it disperses in all directions, ultimately affecting the reflectivity in a quasiperiodic fashion.

IV. CONCLUSIONS AND SUMMARY

We have presented a proof-of-principle method of controlling the magnitude of quantum reflection of a ${}^3\text{He}$ atom from a

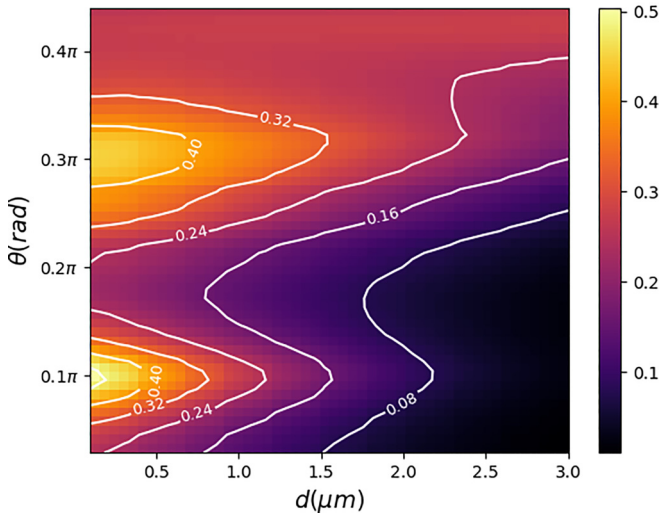


FIG. 8. Reflectivity R as a function of the diameter of the hole, d , and the angle of incidence θ for an atom of Na traveling at $v = 0.1 \text{ m s}^{-1}$.

perfectly reflecting plate by adding a circular hole of varying diameter at its center. The addition of the hole significantly modifies the potential experienced by the atom and directly influences the probability of quantum reflection. We extended the parameter space familiar from standard quantum reflection approaches by allowing our matter wave to travel at arbitrary incidence angles with respect to the surface. This introduces complications as the lack of a chosen single trajectory impacts the choice of boundary conditions in the time-independent approach, rendering defining a suitable-for-all simulation space computationally infeasible. We thus have modeled the problem as a 2D pulse propagation in the presence of an attractive potential and solved a TDSE using a split-step method, utilizing an open source solver [49].

Our results confirm the intuitions insofar as the increase in the hole diameter reduces the probability of the reflection—this is additionally influenced by the coupling between the direction of propagation and the strength of the potential gradient. The ability to study the reflection from the perspective of different directions of propagation reveals varied and interesting behaviors for the same atom. In the Appendix we show how the finer grid density leads to convergence for the case of a normal incidence, and this will naturally apply to arbitrary direction of propagation.

The length scale at which we tested quantum reflection is ideally suited to the regime of nanotechnology, opening up possibilities for designing tunable quantum reflection devices, such as velocity selectors able to filter out neutral atoms [55]. As well as the range of possibilities in technological applications, the plate with the hole offers an interesting scheme for investigating the quantum nature of matter waves. In this paper, we have discussed the behavior of a single atom incident on the perfectly reflecting surface, but the same method (perhaps at lower energies and thus considering retarded distances) can be applied to studying the quantum reflection of a Bose-Einstein condensate, with the specific emphasis on the two-dimensional profiles, which will be explored in a future work. Alternative avenues exist to extend and interpolate the

plate with the hole potential to a nonelectrostatic regime in the form of a heuristic argument as it is often done in dispersion force calculations [17] or numerical simulations. Both remain to be respectively tested to expand the reach of possible quantum reflection experiments.

ACKNOWLEDGMENTS

It is a pleasure to thank M. Caffrey for discussions. Financial support from U.K. Research and Innovation Grant No. EPSRC/DTP 2020/21/EP/T517896/1 is gratefully acknowledged.

APPENDIX

1. Convergence

As already pointed out by Galiffi *et al.* [45], the convergence of a solution to the 2D pulse propagation problem depends on the density of points along the axis of the particle's propagation. They report using different grids for x and y values—the pulse is traveling only along the x axis (normal incidence). In our case of arbitrary incidence, shortening the grid in the y direction leads to spurious results, i.e., the direction of the pulse acquiring a phase of -2θ , where θ is the angle of incidence. As there is no preferred direction of motion, we thus use grids that have equal density across z and ρ . We have inspected the animations of our simulations to establish a lower bound on the number of grid points N , for which the pulse follows a correct trajectory, and we have found it to be 2^{11} . Furthermore, we tested more dense grid configurations of the form $n \times n$ and were limited by memory to the case of $N = 2^{13}$. Thus, we performed the numerical simulations—results of which are shown in Figs. 5–8—using the z grid of $N_z = 2^{12}$, balancing accuracy and performance. Moreover, the algorithm of the split-step numerical method converges for small values of t [49]—in our case the time step was chosen to be $dt = 0.005$.

It is worth noting that introducing the regularization of the potential in the form of a cutoff length ϵ has an influence on overall results. With decreasing ϵ , the potential gradient a particle is experiencing becomes larger, and a denser grid is needed for more accurate sampling. We tested this relationship using our algorithm for the case of normal incidence for different hole diameters, as shown in Fig. 9. The number of points on the ρ axis was fixed to $N_\rho = 2^7$, and we varied the density in the z direction between $N_z = 2^{11}$ and $N_z = 2^{15}$. The values of the cutoff length ϵ are bound by the reflection distance z_R and were chosen between 1 and 5 nm—shown as separate panels in Fig. 9. In each case, we observe that the amplitude of fluctuations around a mean value (dashed line) decreases as the number of points is increased. For increasing diameter d , the oscillations also decrease; the presence of the hole weakens the magnitude of the gradient in the normal direction. Thus, even a smaller resolution is able to capture the behavior adequately. For our choice of the range of ϵ , the oscillations decrease in a similar manner until $\epsilon = 10 \text{ nm}$, where they become more smoothed out for $N_z > 2^{14}$.

All numerical computations were performed on a PC with an eight-core 11th Gen Intel(R) Core(TM) i7-11700 at

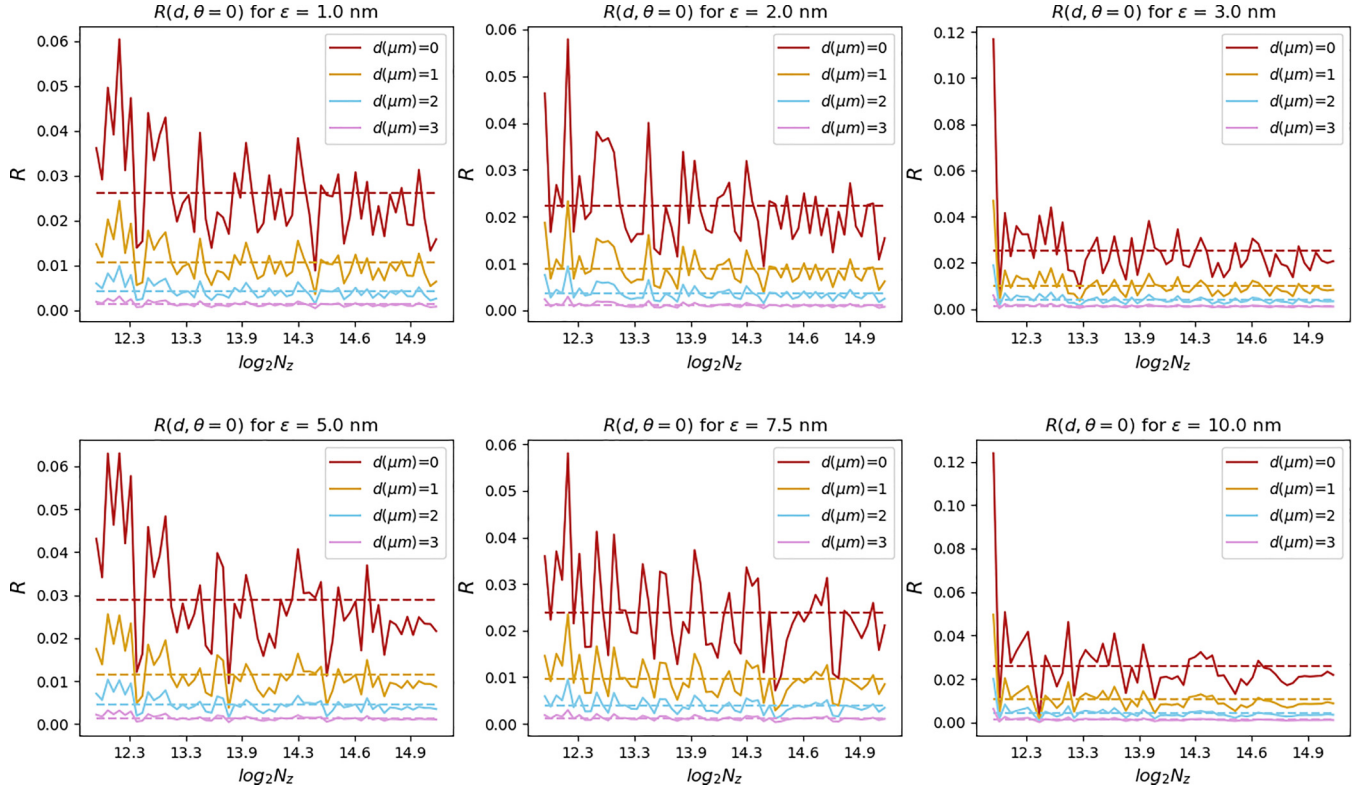


FIG. 9. Relationship between reflectivity R and grid density in the z direction for normal incidence for the ^3He atom. The number of points on the ρ axis is kept constant, $N_\rho = 2^7$. Different colored lines (also appearing on the plots in a sequential order of increasing d) correspond to different diameters of the hole—which when increased reduce reflectivity as well as the magnitude of the fluctuations.

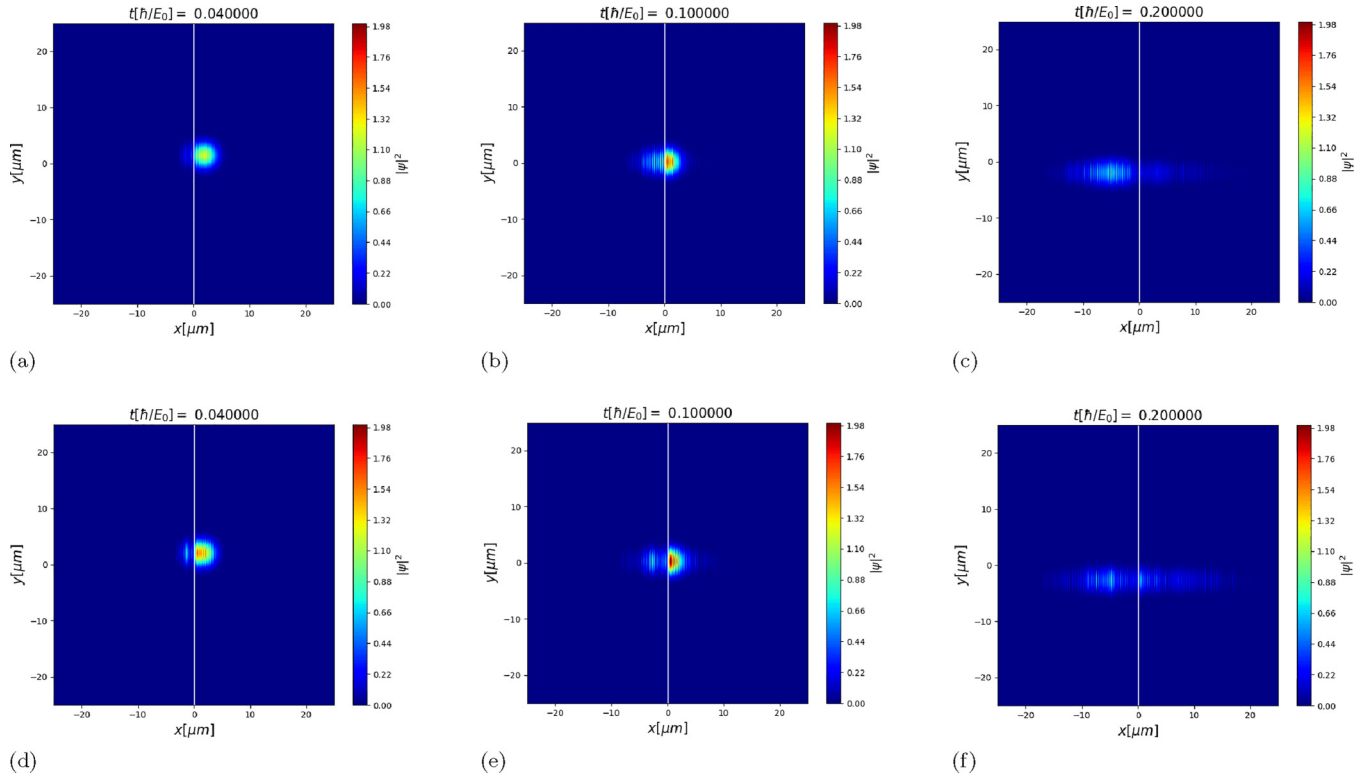


FIG. 10. Different stages ($t = 0.04, 0.1$, and 0.2) of the wave-packet propagation and scattering for the Na atom at a plate without a hole. The top row shows low reflectivity—resultant from propagation at angle $\theta = 0.2\pi$, whereas the bottom row depicts high reflectivity—angle $\theta = 0.3\pi$. The standard deviations σ_ρ and σ_z have been increased to 2 for ease of distinguishing the wave-packet features.

2.50 GHz, 16 GB of RAM, and a Rocky Linux operating system.

2. Periodic behavior

We have examined the animations produced by the simulations and found the visual representation to agree with the calculated values of reflectivity. The plots can be seen in Fig. 10; there, we have included snapshots from the simulations of the Na atom where angles of incidence were respectively $\theta = 0.2\pi$ and $\theta = 0.3\pi$. The respective resultant

reflectivities $R(t_f)$ were 0.221 and 0.353, which agree with the main results, leading us to assume that the reflectivity calculations are correct for all θ . The influence of θ on periodic behavior seen in Figs. 6 and 8 cannot be explained through the action of simple functions such as $\sin\theta$ ($\cos\theta$) since they are strictly increasing (decreasing) on the interval $(0, \frac{\pi}{2})$. Thus, a more complicated response must be at play, being born out of the scattering of the wave packet across different angles of incidence. Given the strong nonseparability of Eq. (14), we are unable to investigate this behavior analytically.

-
- [1] V. L. Pokrovskii, S. K. Savvinykh, and F. R. Ulinich, Reflection from a barrier in the quasi-classical approximation, *Zh. Eksp. Teor. Fiz.* **34**, 1272 (1958) [*J. Exp. Theor. Phys.* **7**, 879 (1958)].
- [2] L. Brekhovskikh, *Waves in Layered Media*, 2nd ed. (Elsevier, Amsterdam, 2012), p. 7.
- [3] J. E. Lennard-Jones and A. F. Devonshire, The interaction of atoms and molecules with solid surfaces III—The condensation and evaporation of atoms and molecules, *Proc. R. Soc. London, Ser. A* **156**, 66 (1936).
- [4] B. S. Zhao, G. Meijer, and W. Schöllkopf, Quantum reflection of He₂ several nanometers above a grating surface, *Science* **331**, 892 (2011).
- [5] N. T. Maitra and E. J. Heller, Semiclassical perturbation approach to quantum reflection, *Phys. Rev. A* **54**, 4763 (1996).
- [6] D. O. Edwards and P. P. Fatouros, Theory of atomic scattering at the free surface of liquid ⁴He, *Phys. Rev. B* **17**, 2147 (1978).
- [7] C. Henkel, C. I. Westbrook, and A. Aspect, Quantum reflection: atomic matter-wave optics in an attractive exponential potential, *J. Opt. Soc. Am. B* **13**, 233 (1996).
- [8] B. Segev, R. Cote, and M. Raizen, Quantum reflection from an atomic mirror, *Phys. Rev. A* **56**, R3350 (1997).
- [9] C. Eltschka, M. J. Moritz, and H. Friedrich, Near-threshold quantization and scattering for deep potentials with attractive tails, *J. Phys. B: At., Mol. Opt. Phys.* **33**, 4033 (2000).
- [10] G. Rojas-Lorenzo, J. Rubayo-Soneira, S. Miret-Artés, and E. Pollak, Quantum threshold reflection of He-atom beams from rough surfaces, *Phys. Rev. A* **101**, 022506 (2020).
- [11] H. Friedrich, G. Jacoby, and C. G. Meister, Quantum reflection by Casimir–van der Waals potential tails, *Phys. Rev. A* **65**, 032902 (2002).
- [12] G. Dufour, R. Guérout, A. Lambrecht, V. V. Nesvizhevsky, S. Reynaud, and A. Y. Voronin, Quantum reflection of antihydrogen from nanoporous media, *Phys. Rev. A* **87**, 022506 (2013).
- [13] P.-P. Crépin, E. A. Kupriyanova, R. Guérout, A. Lambrecht, V. V. Nesvizhevsky, S. Reynaud, S. Vasiliev, and A. Y. Voronin, Quantum reflection of antihydrogen from a liquid helium film, *Europhys. Lett.* **119**, 33001 (2017).
- [14] Y.-P. Bai, J.-L. Li, G.-R. Wang, and S.-L. Cong, Model for investigating quantum reflection and quantum coherence in ultracold molecular collisions, *Phys. Rev. A* **100**, 012705 (2019).
- [15] Y. Ou, Q. Zhang, and G. Huang, Quantum reflection of single photons in a cold Rydberg atomic gas, *Opt. Lett.* **47**, 4395 (2022).
- [16] Z. Bai, Q. Zhang, and G. Huang, Quantum reflections of nonlocal optical solitons in a cold Rydberg atomic gas, *Phys. Rev. A* **101**, 053845 (2020).
- [17] F. Shimizu, Specular reflection of very slow metastable neon atoms from a solid surface, *Phys. Rev. Lett.* **86**, 987 (2001).
- [18] B. S. Zhao, G. Meijer, and W. Schöllkopf, Emerging beam effects in out-of-plane grating diffraction of He atom beams, *New J. Phys.* **13**, 065017 (2011).
- [19] V. Druzhinina and M. DeKieviet, Experimental observation of quantum reflection far from threshold, *Phys. Rev. Lett.* **91**, 193202 (2003).
- [20] A. Jurisch and J.-M. Rost, Trapping cold atoms by quantum reflection, *Phys. Rev. A* **77**, 043603 (2008).
- [21] T. A. Pasquini, M. Saba, G.-B. Jo, Y. Shin, W. Ketterle, D. E. Pritchard, T. A. Savas, and N. Mulders, Low velocity quantum reflection of Bose-Einstein condensates, *Phys. Rev. Lett.* **97**, 093201 (2006).
- [22] D.-M. Wang, J.-C. Xing, R. Du, B. Xiong, and T. Yang, Quantum reflection of a Bose-Einstein condensate with a dark soliton from a step potential, *Chin. Phys. B* **30**, 120303 (2021).
- [23] B. S. Zhao, S. A. Schulz, S. A. Meek, G. Meijer, and W. Schöllkopf, Quantum reflection of helium atom beams from a microstructured grating, *Phys. Rev. A* **78**, 010902(R) (2008).
- [24] H. Gies, F. Karbstein, and N. Seeger, Quantum reflection as a new signature of quantum vacuum nonlinearity, *New J. Phys.* **15**, 083002 (2013).
- [25] S. Y. Buhmann, *Dispersion Forces I: Macroscopic Quantum Electrodynamics and Ground-State Casimir, Casimir-Polder and van der Waals Forces*, Springer Tracts in Modern Physics Vol. 247 (Springer, Berlin, 2012).
- [26] R. Eisenschitz and F. London, Über das Verhältnis der van der Waalsschen kräfte zu den homöopolaren Bindungskräften, *Z. Angew. Phys.* **60**, 491 (1930).
- [27] H. B. G. Casimir, On the attraction between two perfectly conducting plates, *Indag. Math.* **10**, 261 (1948).
- [28] E. M. Lifshitz and M. Hamermesh, The theory of molecular attractive forces between solids, *Perspectives in Theoretical Physics*, edited by L. P. Pitaevski (Pergamon, Amsterdam, 1992), pp. 329–349.
- [29] J. E. Lennard-Jones, Processes of adsorption and diffusion on solid surfaces, *Trans. Faraday Soc.* **28**, 333 (1932).
- [30] H. B. G. Casimir and D. Polder, The influence of retardation on the London-van der Waals forces, *Phys. Rev.* **73**, 360 (1948).
- [31] M. Silvestre, T. P. Cysne, D. Szilard, F. A. Pinheiro, and C. Farina, Tuning quantum reflection in graphene with an external magnetic field, *Phys. Rev. A* **100**, 033605 (2019).

- [32] T. Cysne, W. J. M. Kort-Kamp, D. Oliver, F. A. Pinheiro, F. S. S. Rosa, and C. Farina, Tuning the Casimir-Polder interaction via magneto-optical effects in graphene, *Phys. Rev. A* **90**, 052511 (2014).
- [33] W.-K. Tse and A. H. MacDonald, Quantized Casimir force, *Phys. Rev. Lett.* **109**, 236806 (2012).
- [34] T. P. Cysne, T. G. Rappoport, A. Ferreira, J. M. V. P. Lopes, and N. M. R. Peres, Numerical calculation of the Casimir-Polder interaction between a graphene sheet with vacancies and an atom, *Phys. Rev. B* **94**, 235405 (2016).
- [35] N. S. Nichols, A. Del Maestro, C. Wexler, and V. N. Kotov, Adsorption by design: Tuning atom-graphene van der Waals interactions via mechanical strain, *Phys. Rev. B* **93**, 205412 (2016).
- [36] N. Khusnutdinov, R. Kashapov, and L. M. Woods, Casimir-Polder effect for a stack of conductive planes, *Phys. Rev. A* **94**, 012513 (2016).
- [37] K. Sulimany, O. Lib, G. Masri, A. Klein, M. Fridman, P. Grelu, O. Gat, and H. Steinberg, Bidirectional soliton rain dynamics induced by Casimir-like interactions in a graphene mode-locked fiber laser, *Phys. Rev. Lett.* **121**, 133902 (2018).
- [38] A. A. Banishev, H. Wen, J. Xu, R. K. Kawakami, G. L. Klimchitskaya, V. M. Mostepanenko, and U. Mohideen, Measuring the Casimir force gradient from graphene on a SiO₂ substrate, *Phys. Rev. B* **87**, 205433 (2013).
- [39] M. Liu, Y. Zhang, G. L. Klimchitskaya, V. M. Mostepanenko, and U. Mohideen, Demonstration of an unusual thermal effect in the Casimir force from graphene, *Phys. Rev. Lett.* **126**, 206802 (2021).
- [40] P. P. Abrantes, T. P. Cysne, D. Szilard, F. S. S. Rosa, F. A. Pinheiro, and C. Farina, Probing topological phase transitions via quantum reflection in the graphene family materials, *Phys. Rev. B* **104**, 075409 (2021).
- [41] A. R. Barnea, B. A. Stickler, O. Cheshnovsky, K. Hornberger, and U. Even, Electrically controlled quantum reflection, *Phys. Rev. A* **95**, 043639 (2017).
- [42] C. Eberlein and R. Zietal, Casimir-Polder interaction between a polarizable particle and a plate with a hole, *Phys. Rev. A* **83**, 052514 (2011).
- [43] A. Mody, M. Haggerty, J. M. Doyle, and E. J. Heller, No-sticking effect and quantum reflection in ultracold collisions, *Phys. Rev. B* **64**, 085418 (2001).
- [44] H. Friedrich and J. Trost, Working with WKB waves far from the semiclassical limit, *Phys. Rep.* **397**, 359 (2004).
- [45] E. Galiffi, C. Sünderhauf, M. DeKieviet, and S. Wimberger, Two-dimensional simulation of quantum reflection, *J. Phys. B: At., Mol. Opt. Phys.* **50**, 095001 (2017).
- [46] B. Kelvin, William Thomson, J. Larmor, and J. P. Joule, *Mathematical and Physical Papers* (Cambridge University, Cambridge, England, 1841–1907), collected from different scientific periodicals from May, 1841, to the present time.
- [47] G. Vidali, G. Ihm, H.-Y. Kim, and M. W. Cole, Potentials of physical adsorption, *Surf. Sci. Rep.* **12**, 135 (1991).
- [48] B. Herwerth, M. DeKieviet, J. Madroñero, and S. Wimberger, Quantum reflection from an oscillating surface, *J. Phys. B: At., Mol. Opt. Phys.* **46**, 141002 (2013).
- [49] E. Figueiras, D. Olivieri, A. Paredes, and H. Michinel, An open source virtual laboratory for the Schrödinger equation, *Eur. J. Phys.* **39**, 055802 (2018).
- [50] G. P. Agrawal, *Nonlinear Fiber Optics*, 4th ed. (Academic Press, Burlington, MA, 2007).
- [51] M. V. Berry and K. E. Mount, Semiclassical approximations in wave mechanics, *Rep. Prog. Phys.* **35**, 315 (1972).
- [52] G. Dufour, A. Gérardin, R. Guérout, A. Lambrecht, V. V. Nesvizhevsky, S. Reynaud, and A. Y. Voronin, Quantum reflection of antihydrogen from the Casimir potential above matter slabs, *Phys. Rev. A* **87**, 012901 (2013).
- [53] A. Derevianko, W. R. Johnson, M. S. Safronova, and J. F. Babb, High-precision calculations of dispersion coefficients, static dipole polarizabilities, and atom-wall interaction constants for alkali-metal atoms, *Phys. Rev. Lett.* **82**, 3589 (1999).
- [54] A. Vander Vorst, A. Rosen, and Y. Kotsuka, *RF/Microwave Interaction with Biological Tissues* (Wiley & Sons, New York, 2006).
- [55] P. Solař, J. Kousal, J. Hanus, K. Škorvánková, A. Kuzminova, and O. Kylián, Mechanical time-of-flight filter based on slotted disks and helical rotor for measurement of velocities of nanoparticles, *Sci. Rep.* **11**, 6415 (2021).